

Cite this: *RSC Adv.*, 2015, 5, 4109

Photoluminescence, photocatalysis and Judd–Ofelt analysis of Eu^{3+} -activated layered BiOCl phosphors†

Rohit Saraf,^a C. Shivakumara,^{*a} Sukanti Behera,^a H. Nagabhushana^b and N. Dhananjaya^c

Eu^{3+} -activated layered BiOCl phosphors were synthesized by the conventional solid-state method at relatively low temperature and shorter duration (400 °C for 1 h). All the samples were crystallized in the tetragonal structure with the space group $P4/nmm$ (no. 129). Field emission scanning electron microscopy (FE-SEM) studies confirmed the plate-like morphology. Photoluminescence spectra exhibit characteristic luminescent $^5\text{D}_0 \rightarrow ^7\text{F}_J$ ($J = 0-4$) intra-4f shell Eu^{3+} ion transitions. The electric dipole transition located at 620 nm ($^5\text{D}_0 \rightarrow ^7\text{F}_2$) was stronger than the magnetic dipole transition located at 594 nm ($^5\text{D}_0 \rightarrow ^7\text{F}_1$). The evaluated Commission International de l'Eclairage (CIE) color coordinates of Eu^{3+} -activated BiOCl phosphors were close to the commercial $\text{Y}_2\text{O}_3:\text{Eu}^{3+}$ and $\text{Y}_2\text{O}_2\text{S}:\text{Eu}^{3+}$ red phosphors. Intensity parameters (Q_2 , Q_4) and various radiative properties such as transition probability (A_{tot}), radiative lifetime (τ_{rad}), stimulated emission cross-section (σ_e), gain bandwidth ($\sigma_e \times \Delta\lambda_{\text{eff}}$) and optical gain ($\sigma_e \times \tau_{\text{rad}}$) were calculated using the Judd–Ofelt theory. The experimental decay curves of the $^5\text{D}_0$ level in Eu^{3+} -activated BiOCl have a single exponential profile. In comparison with other Eu^{3+} doped materials, Eu^{3+} -activated BiOCl phosphors have a long lifetime (τ_{exp}), low non-radiative relaxation rate (W_{NR}), high quantum efficiency (η) and better optical gain ($\sigma_e \times \tau_{\text{rad}}$). The determined radiative properties revealed the usefulness of Eu^{3+} -activated BiOCl in developing red lasers as well as optical display devices. Further, these samples showed efficient photocatalytic activity for the degradation of rhodamine B (RhB) dye under visible light irradiation. These photocatalysts are useful for the removal of toxic and non-biodegradable organic pollutants in water.

Received 10th September 2014

Accepted 1st December 2014

DOI: 10.1039/c4ra10163d

www.rsc.org/advances

1. Introduction

The unique spectroscopic properties of rare-earth ions in different host lattices prompted the development of rare-earth luminescent materials for lamps, cathode ray tubes, radiation monitoring systems, lasers, scintillators, biosensors and white light-emitting diodes (WLEDs).^{1,2} White light-emitting diodes are potential materials for significantly improving lighting efficiency, resulting in reduction of the excitation energy and also reduction in pollution from fossil fuel power plants.³ The demand for developing efficient luminescent materials such as rare earth activated inorganic compounds has attracted researchers. Due to their possible photonic applications, good luminescent characteristics, stability in high vacuum,

biosensors and absence of corrosive gas emission under electron bombardment when compared to currently used sulfide based phosphors. Among all the rare-earth ions, the red emitting trivalent Eu^{3+} -activated phosphors have significant importance because of their potential application in color display and lighting technologies. Trivalent europium ions (Eu^{3+}) activated phosphors were considered to obtain a red-emitting phosphor with proper CIE chromaticity coordinates. This was because the lowest excited level ($^5\text{D}_0$) of the $4f^6$ configuration in Eu^{3+} was situated below the $4f^55d$ configuration. Eu^{3+} provides a particularly favorable situation for substitution in Bi^{3+} sites with suitable isostructural replacement. Trivalent europium ions exhibited narrow band emissions, long lifetimes and large Stokes shifts (emission of lower energy radiation upon excitation by higher energy radiation). The intensities and splitting of the spectral lines provide useful information concerning the local site symmetry, sizes of cations and properties of the chemical bonding.⁴ Eu^{3+} ions exhibit intense $^5\text{D}_0 \rightarrow ^7\text{F}_2$ emission in the red spectral region at 615 nm, when they occupy the lattice sites without centrosymmetry.

Bismuth oxychloride (BiOCl) belongs to V-VI-VII family, an important ternary phosphor among various inorganic phosphors due to their unique layered structures and high chemical

^aSolid State and Structural Chemistry Unit, Indian Institute of Science, Bangalore 560012, India. E-mail: shiva@sscu.iisc.ernet.in; Fax: +91-80-2360-1310; Tel: +91-80-2293-2951

^bC. N. R. Rao Center for Advanced Materials, Tumkur University, Tumkur 572 103, India

^cDepartment of Physics, B.M.S. Institute of Technology, Bangalore 560 064, India

† Electronic supplementary information (ESI) available. See DOI: 10.1039/c4ra10163d

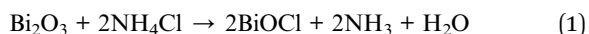
stability.⁴ Oxyhalides-based phosphors would be advantageous when compared to oxidic hosts due to their low phonon energy, which improved the quantum efficiency of the luminescence. BiOCl compound crystallize in the tetragonal matlockite (PbFCl) structure with [Cl–Bi–O–Bi–Cl] layers stacked together by nonbonding van der Waals interaction through the halogen atoms along *c*-axis.⁵ Due to the strong intralayer bonding and weak interlayer van der Waals interaction, BiOCl show promising applications in photocatalysis, pharmaceuticals, battery cathodes, and photoelectrochemical devices.^{6,7} The internal static electric fields between these layers enable the effective separation of photogenerated electron–hole pairs. Moreover, the electron–hole recombination was prohibited due to the indirect band gap nature of BiOCl where the excited electron in conduction band has to gain the crystal momentum in *k*-space with the emission or absorption of phonon before annihilating a hole in valence band radiatively.⁸ Several methods were employed for the synthesis of BiOCl, namely hydrothermal,⁹ hydrolysis,¹⁰ sonochemical,¹¹ reverse microemulsion,¹² microwave⁴ and chemical vapor deposition⁷ methods. All these synthesis methods involve several problems, such as high pressure, less yield, lack of composition control, requirement of solvents and long reaction time.

Generally, solid state method offer several advantages over other conventional methods such as mass scale production, higher purity of products, better compositional control and solvent/surfactant free process. As per our knowledge, the spectroscopic properties of Eu³⁺-activated BiOCl have not been extensively reported so far and need careful examination. In the present study, we employed solid state method to prepare Eu³⁺-activated BiOCl compounds and reported their structural and optical parameters. The effect of Eu³⁺ concentration on photoluminescence (PL) properties was investigated. Judd–Ofelt theory was adopted to calculate the intensity parameters and various other radiative properties such as transition probability, radiative life time, quantum efficiency, stimulated emission cross-section, gain bandwidth and optical gain. Further, these compounds were used as photocatalysts for the degradation of rhodamine B (RhB) dye under visible light irradiation.

2. Experimental

2.1. Synthesis

Bi_{1-x}Eu_xOCl (*x* = 0, 0.01, 0.03 and 0.05) compounds were synthesized by conventional solid-state method. For the synthesis of host BiOCl, the required amount of Bi₂O₃ (1.1649 g) and NH₄Cl (0.3209 g, 20% excess) were used as the starting materials and were ground finely in an agate mortar with pestle. This mixed powder was transferred into crucible and calcined at 400 °C for 1 h. Similarly, Eu³⁺-activated BiOCl compounds were synthesized using Bi₂O₃, Eu₂O₃ and NH₄Cl as the raw materials. The equation for the formation of BiOCl compound was represented by the following reaction:



2.2. Characterization

The crystallinity and phase purity of the samples were examined by powder X-ray diffraction (PANalytical X'Pert Pro Powder diffractometer) using Cu K α radiation ($\lambda = 1.5418 \text{ \AA}$) with a nickel filter. Rietveld refinement data were collected at a scan rate of 1° min^{-1} with a 0.02° step size for 2θ from 10° to 80° . The structural parameters were estimated by Rietveld refinement method using FullProf Suite-2000 programme. The surface morphology and elemental mapping of these phosphors was investigated using FE-SEM (FEI Sirion). Fourier transform infrared (FTIR) spectra were recorded using Perkin Elmer Spectrometer, Frontier using KBr as a reference. UV-Visible absorption spectra have been recorded for powders on Perkin Elmer Lambda 750 spectrophotometer. Thermogravimetric analysis (TGA) was performed using Mettler-Toledo system in the presence of N₂ as a carrier gas upto 900 °C. The PL studies have been carried out using a JobinYvon spectrofluorometer (Fluorolog-3, Horiba) equipped with a 450 W xenon lamp as the excitation source. The photoluminescence (PL) decay lifetime measurements were performed at low temperature (77 K) with a Perkin Elmer spectrofluorimeter. The photocatalytic activity of rhodamine B (RhB) dye solution was analyzed by Perkin Elmer UV-Visible spectrophotometer (Lambda 35) in the range from 200 to 800 nm periodically. All the measurements were performed at room temperature.

2.3. Photocatalytic activity measurement

The photocatalytic activities of Bi_{1-x}Eu_xOCl compounds were measured by examining the degradation of RhB dye under visible-light irradiation ($\lambda > 420 \text{ nm}$). A 500 W metal halide lamp held at 15 cm from the sample was used as the visible-light source. In each experiment, about 50 mg of photocatalysts was added into 50 mL of RhB solution with a concentration of $5 \times 10^{-6} \text{ M}$. Prior to Visible illumination, the suspensions were magnetically stirred in the dark for 30 minutes to ensure an adsorption–desorption equilibrium. Then, the stable aqueous dye solution was exposed to visible light for 45 minutes. During the photoreaction, about 3 mL of suspension was collected at different time intervals and centrifuged to remove the catalyst. The transparent solution was analyzed using a UV-Vis spectrophotometer, and the absorbance was measured at a wavelength of 554 nm, which corresponds to the maximum absorption wavelength of RhB. The percentage dye degradation rate was calculated by the following equation:

$$\text{Degradation efficiency}(\%) = \frac{C_0 - C}{C_0} \times 100 \quad (2)$$

where C_0 is the initial concentration at 0 min and C is the concentration at time t .

3. Results and discussion

3.1. Powder X-ray diffraction (PXRD)

Fig. 1 shows the indexed powder X-ray diffraction patterns for Bi_{1-x}Eu_xOCl compounds. The sharp intense peaks revealed the crystalline nature of the samples. All diffracted peaks were agreed well with the reported JCPDS Card no. 85-0861. On substitution of

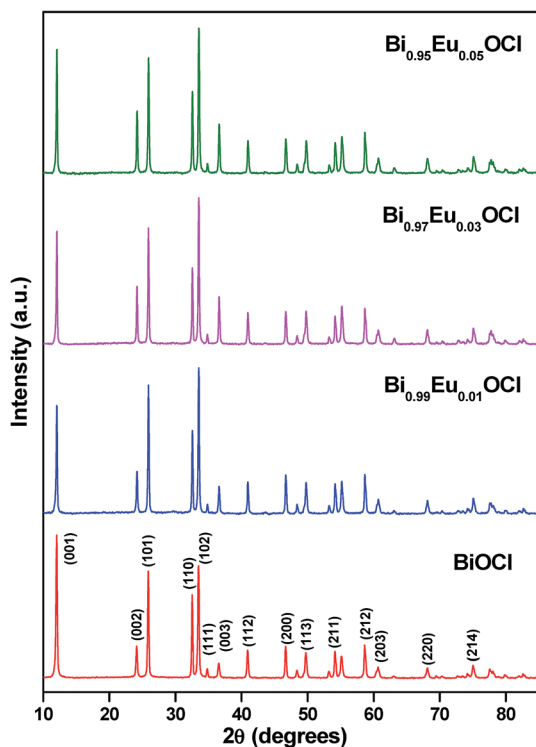


Fig. 1 XRD patterns of $\text{Bi}_{1-x}\text{Eu}_x\text{OCl}$ compounds.

smaller Eu^{3+} ion ($r_{\text{Eu}^{3+}} = 1.066 \text{ \AA}$) to larger Bi^{3+} ion ($r_{\text{Bi}^{3+}} = 1.17 \text{ \AA}$) upto 5 mol%, we did not see any impurity line of Eu_2O_3 in the powder XRD patterns. This implies that the Eu^{3+} substituted to 8-coordinated Bi^{3+} ion in BiOCl lattice. On substitution of Eu^{3+} ion, we did not see any appreciable change in the intensity of diffracted lines. The structural parameters were refined from the Rietveld method using powder XRD data. The refinement results confirmed that all the samples were crystallized in the tetragonal phase with space group $P4/nmm$ (no. 129) and the structural parameters were summarized in Table 1. It was noted that there was no appreciable change in the lattice parameters or cell volume upto 5 mol% substitution of Eu^{3+} ion. Observed, calculated and the difference XRD pattern of $\text{Bi}_{0.97}\text{Eu}_{0.03}\text{OCl}$ compound is shown in Fig. 2a. The crystal structure of BiOCl was modeled using Rietveld refined structural parameters by VESTA program (Fig. 2b). In the BiOCl structure, the Bi^{3+} atom was coordinated to a square antiprism with four O atoms in one base and four Cl atoms in another base. The BiOCl layers were stacked over one another by the nonbonding van der Waals interaction through chloride atoms along the c -axis. The interplanar lattice spacing between two bismuth ions in BiOCl layers was found to be 4.85 \AA .

3.2. Field emission scanning electron microscopy (FE-SEM) analysis

Fig. 3 shows FE-SEM images of BiOCl and $\text{Bi}_{0.95}\text{Eu}_{0.05}\text{OCl}$ compounds. The micrographs revealed the plate-like

Table 1 Rietveld refined structural parameters for $\text{Bi}_{1-x}\text{Eu}_x\text{OCl}$ compounds

Compounds	BiOCl	$\text{Bi}_{0.99}\text{Eu}_{0.01}\text{OCl}$	$\text{Bi}_{0.97}\text{Eu}_{0.03}\text{OCl}$	$\text{Bi}_{0.95}\text{Eu}_{0.05}\text{OCl}$
Crystal system	Tetragonal	Tetragonal	Tetragonal	Tetragonal
Space group	$P4/nmm$ (no. 129)	$P4/nmm$ (no. 129)	$P4/nmm$ (no. 129)	$P4/nmm$ (no. 129)
Lattice parameters				
a (\AA)	3.893(2)	3.894(2)	3.895(3)	3.895(2)
c (\AA)	7.366(3)	7.374(3)	7.372(7)	7.371(5)
Cell volume (\AA^3)	111.63(8)	111.81(3)	111.85(2)	111.82(1)
Atomic positions				
Bi/Eu (2c)				
x	0.2500	0.2500	0.2500	0.2500
y	0.2500	0.2500	0.2500	0.2500
z	0.1707(2)	0.1703(3)	0.1704(7)	0.1703(5)
O (2a)				
x	0.2500	0.2500	0.2500	0.2500
y	0.7500	0.7500	0.7500	0.7500
z	0.0000	0.0000	0.0000	0.0000
Cl (2c)				
X	0.2500	0.2500	0.2500	0.2500
Y	0.2500	0.2500	0.2500	0.2500
z	0.6447(9)	0.6560(8)	0.6479(5)	0.6535(5)
R_{factors} (%)				
R_p	0.103	0.127	0.124	0.118
R_{wp}	0.141	0.168	0.171	0.160
R_{exp}	0.119	0.135	0.156	0.148
χ^2	0.013	0.016	0.012	0.012
R_{Bragg}	0.056	0.087	0.065	0.064
R_F	0.035	0.065	0.050	0.047

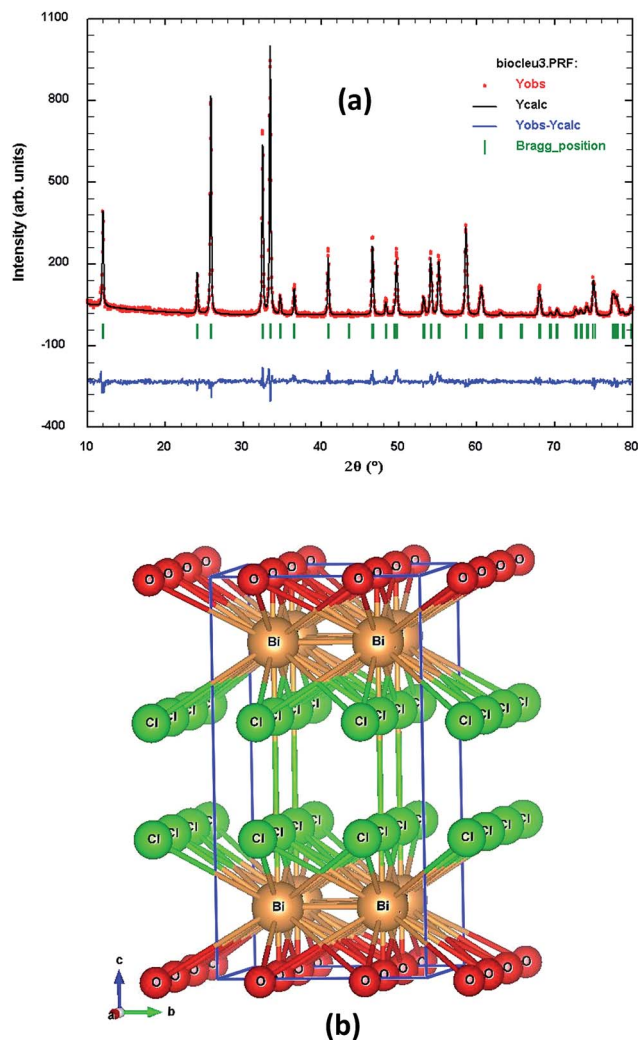


Fig. 2 (a) Observed, calculated and the difference XRD patterns of $\text{Bi}_{0.97}\text{Eu}_{0.03}\text{OCl}$ and (b) crystal structure of BiOCl compound.

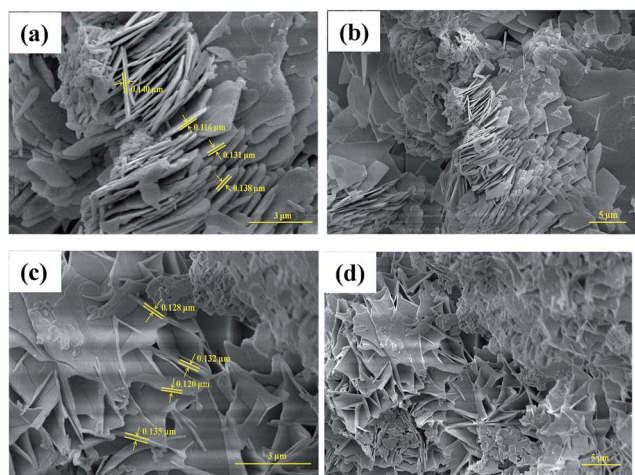


Fig. 3 FESEM micrographs of (a and b) BiOCl and (c and d) $\text{Bi}_{0.95}\text{Eu}_{0.05}\text{OCl}$ compounds.

morphology. Similar morphology was obtained by Wang *et al.*⁶ using hydrolysis method and Li *et al.*⁹ via hydrothermal route. The thickness of the plates in both compounds was found in the range of 0.116–0.140 μm . To confirm the homogeneity of elements in the compounds, we have carried out the elemental mapping using energy dispersive X-ray (EDX) analysis. Fig. 4 shows the elemental mapping of (a) BiOCl and (b) $\text{Bi}_{0.95}\text{Eu}_{0.05}\text{OCl}$ compounds. The elemental mapping of BiOCl confirmed that all the elements were homogeneously distributed over the entire area. For 5 mol% Eu^{3+} doping, although the concentration of Eu was low and therefore faintly visible but was evenly distributed.

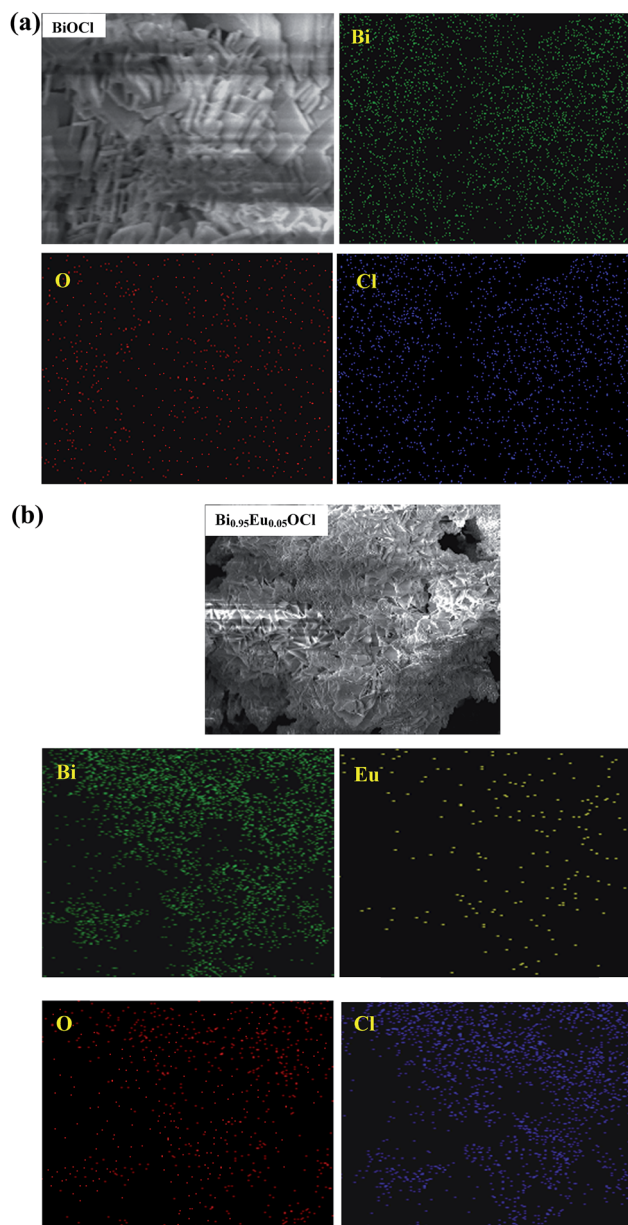


Fig. 4 Elemental mapping of (a) BiOCl and (b) $\text{Bi}_{0.95}\text{Eu}_{0.05}\text{OCl}$ compounds.

3.3. Fourier transform infrared (FTIR) studies

The purity and functional groups of all the compounds were confirmed by the FTIR spectra (Fig. 5). All the samples show absorption peak at 524 cm^{-1} which was attributed to the characteristic symmetrical stretching vibration of the Bi–O bond. Further, we did not observe any additional bands which confirm that all the compounds were pure phase.

3.4. UV-vis absorption spectroscopy

Fig. 6a illustrates the UV-Vis absorption spectra of $\text{Bi}_{1-x}\text{Eu}_x\text{OCl}$ compounds. A red shift was observed in the absorption edge with increasing Eu^{3+} concentration in BiOCl. The optical energy band gap (E_g) was estimated from these absorption spectra using Wood and Tauc relation.¹³ The energy band gap was calculated with absorbance and photon energy by the following equation:

$$\alpha h\nu = A(h\nu - E_g)^n \quad (3)$$

where α is the absorption coefficient, $h\nu$ is the photon energy, A is a proportional constant, E_g is the energy band gap and n depends on the characteristics of the transition in a semiconductor. ($n = 1/2, 2, 3/2$, or 3 for allowed direct, allowed indirect, forbidden direct, and forbidden indirect electronic transitions, respectively). BiOCl exhibits an optical absorption spectrum governed by indirect electronic transitions ($n = 2$).¹⁴ The intercept of the tangent to the x-axis gives good approximation of the band gap energies of $\text{Bi}_{1-x}\text{Eu}_x\text{OCl}$ compounds. The energy band gaps for BiOCl, $\text{Bi}_{0.99}\text{Eu}_{0.01}\text{OCl}$, $\text{Bi}_{0.97}\text{Eu}_{0.03}\text{OCl}$ and $\text{Bi}_{0.95}\text{Eu}_{0.05}\text{OCl}$ were found to be $2.92 (\pm 0.0031)$, $2.90 (\pm 0.0026)$, $2.88 (\pm 0.0024)$ and $2.86 (\pm 0.0017)$ eV, respectively (Fig. 6b). The obtained band gap energy values were comparable with the reported literature.¹⁵ On substitution of smaller Eu^{3+} ion ($r_{\text{Eu}^{3+}} = 1.066\text{ \AA}$) to larger Bi^{3+} ion ($r_{\text{Bi}^{3+}} = 1.17\text{ \AA}$), the band gap values decrease. The influence of Eu^{3+} on the electronic structure of the host material was investigated by calculating

the positions of the conduction band (CB) and valence band (VB) edges using the equation:

$$E_{\text{CB}} = X - E^{\text{C}} - 1/2E_g \quad (4)$$

where E_{CB} is the CB edge of the compound at the point of zero charge, X is the absolute electronegativity of the compound (6.34 eV), E^{C} is the energy of free electrons on the hydrogen scale ($\sim 4.5\text{ eV}$) and E_g is the band gap energy of the compound. The calculated bottom of the CBs and top of the VBs of $\text{Bi}_{1-x}\text{Eu}_x\text{OCl}$ compounds are listed in Table 2. The band gap structures for $\text{Bi}_{1-x}\text{Eu}_x\text{OCl}$ compounds are shown in Fig. 6c. As can be seen, the VB edge potential of $\text{Bi}_{1-x}\text{Eu}_x\text{OCl}$ decreases from 3.30 to 3.27 eV due to the smaller ionic radii of Eu^{3+} ion in the BiOCl lattice.

3.5. Thermogravimetric analysis (TGA)

Thermogravimetric analysis was used to evaluate the stability of BiOCl compound. Fig. S1† shows that no significant weight loss was observed upto $590\text{ }^\circ\text{C}$. This confirms that the BiOCl compound was stable. Above $590\text{ }^\circ\text{C}$, a drastic weight loss around 12% was observed in the range of 590 to $780\text{ }^\circ\text{C}$ due to the decomposition of BiOCl into bismuth oxide and chlorine gas. Further, the decomposition of bismuth oxide was started above $780\text{ }^\circ\text{C}$.

3.6. Photoluminescence (PL) properties

In Fig. 7a, an excitation spectrum was presented for $\text{Bi}_{0.99}\text{Eu}_{0.01}\text{OCl}$ phosphor recorded at $\lambda_{\text{em}} = 620\text{ nm}$. A broad excitation peak at 350 nm (${}^7\text{F}_0 \rightarrow {}^5\text{D}_4$) was observed and this band was due to the $\text{Eu}^{3+}\text{--O}^{2-}$ charge transfer (CT) which arises from the transition of $2p$ electrons of O^{2-} to the empty $4f$ orbitals of Eu^{3+} ions. The peak at 394 nm was observed which correspond to ${}^7\text{F}_0 \rightarrow {}^5\text{D}_3$ transition of Eu^{3+} . The excitation spectrum shows a peak at 466 nm (${}^7\text{F}_0 \rightarrow {}^5\text{D}_2$) due to the intra- $4f$ transitions of Eu^{3+} ions in the host lattice.⁴ The emission spectra obtained for Eu^{3+} -activated BiOCl phosphors under the visible excitation (466 nm) displayed the typical emissions in the $570\text{--}720\text{ nm}$ region (Fig. 7b). The sharp peaks in the emission spectra were correspond to the electronic transitions as ${}^5\text{D}_0 \rightarrow {}^7\text{F}_0$ (580 nm), ${}^5\text{D}_0 \rightarrow {}^7\text{F}_1$ (594 nm), ${}^5\text{D}_0 \rightarrow {}^7\text{F}_2$ ($612, 620\text{ nm}$), ${}^5\text{D}_0 \rightarrow {}^7\text{F}_3$ (651 nm) and ${}^5\text{D}_0 \rightarrow {}^7\text{F}_4$ (698 nm). Fig. S2† depicts the energy level diagram for Eu^{3+} -activated BiOCl phosphors. The presence of unique emission line at 580 nm was due to the $J\text{--}J$ mixing by the crystal field effects.¹⁶ The ${}^5\text{D}_0 \rightarrow {}^7\text{F}_1$ transition peak originates from magnetic dipole transition. In contrast, the radiative transitions from ${}^5\text{D}_0$ to ${}^7\text{F}_2$ and ${}^7\text{F}_4$ levels were electric dipole in character.^{16,17} The ${}^5\text{D}_0 \rightarrow {}^7\text{F}_3$ transition was forbidden from both electric and magnetic dipole considerations. It can also be observed that the relative emission intensity of ${}^5\text{D}_0 \rightarrow {}^7\text{F}_2$ transition was higher than ${}^5\text{D}_0 \rightarrow {}^7\text{F}_1$ transition. This was normally associated with Eu^{3+} ions occupying crystallographic sites without an inversion center.¹⁶ The relative intensities of the emissions fall in the order ${}^5\text{D}_0 \rightarrow {}^7\text{F}_2 > {}^7\text{F}_4 > {}^7\text{F}_1 > {}^7\text{F}_0 > {}^7\text{F}_3$ for all Eu^{3+} -activated BiOCl phosphors (Fig. S3†). Additionally, it was worth noting that the emission intensities increase with the

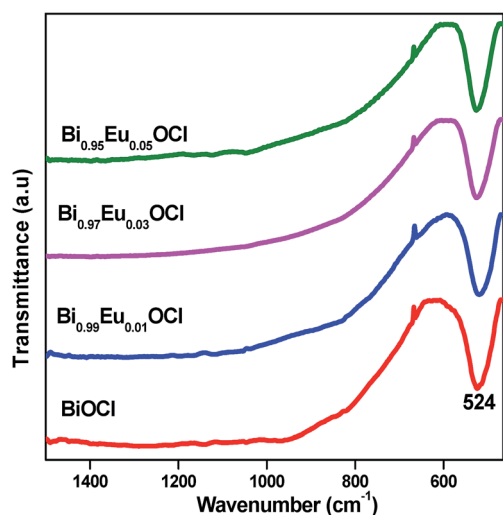


Fig. 5 FTIR spectra of $\text{Bi}_{1-x}\text{Eu}_x\text{OCl}$ compounds.

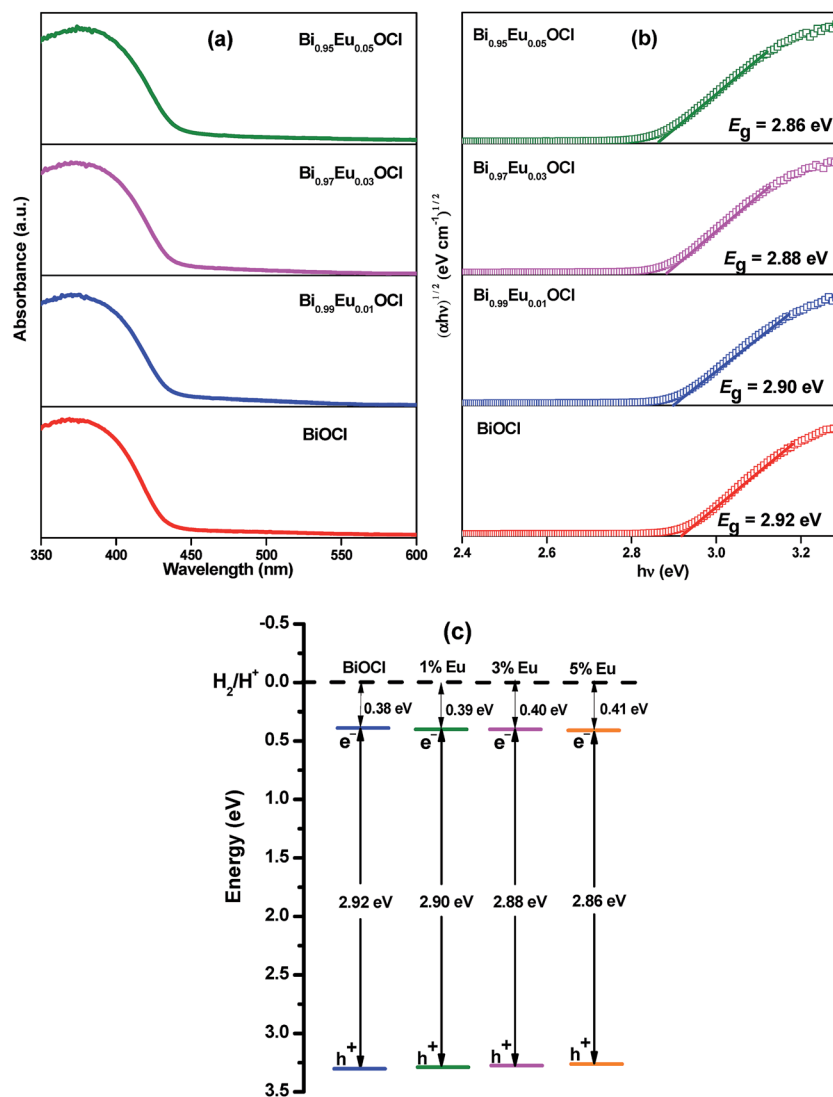


Fig. 6 (a) UV-Vis absorption spectra, (b) plots of $(\alpha h\nu)^{1/2}$ vs. $h\nu$ and (c) band gap structures for Bi_{1-x}Eu_xOCl compounds.

increase in Eu³⁺ doping concentration from 1 to 5 mol%. The splitting of ⁵D₀ → ⁷F₂ peak was due to the composition, coordination environment and crystal field symmetry.¹⁸

For practical lighting applications, color quality was specified in terms of 1931 Commission International de l'Eclairage (CIE) chromaticity color coordinates. These color coordinates recognize that the human visual system uses three primary colors: red, green and blue.¹⁹ In general, the color of any light source can be represented on the (x, y) coordinates in this color space. To characterize the luminescence of Bi_{1-x}Eu_xOCl materials under visible excitation (466 nm), the CIE coordinates were calculated using the color calculator program radiant imaging.²⁰ Fig. 8 shows the CIE 1931 chromaticity diagram of Bi_{1-x}Eu_xOCl phosphors. The calculated CIE color coordinates of Bi_{1-x}Eu_xOCl ($x = 0.01, 0.03$ and 0.05) phosphors were found to be (0.6193, 0.3802), (0.6322, 0.3653) and (0.6371, 0.3615), respectively. The evaluated color coordinates for Bi_{0.95}Eu_{0.05}OCl phosphor was close to the commercial Y₂O₃:Eu³⁺ (0.645, 0.347) and Y₂O₂S:Eu³⁺ (0.647, 0.343) red phosphors.²¹ The location of

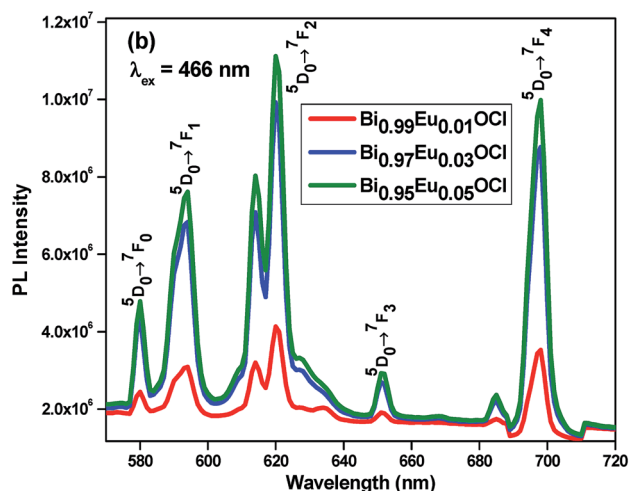
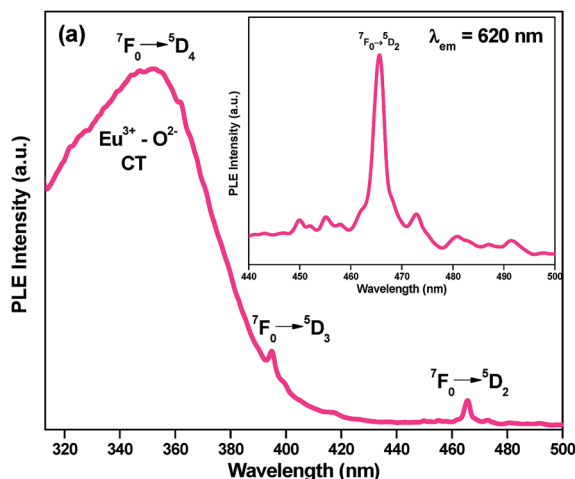
the color coordinates of Eu³⁺-activated BiOCl on the CIE chromaticity diagram presented in Fig. 8 revealed that the color properties of the phosphor materials can be useful for the production of red component in white LEDs.

3.7. Judd–Ofelt intensity parameters and radiative properties

The PL emission spectrum was further used for the calculation of Judd–Ofelt parameters. The J–O intensity parameters, Ω_f ($f = 2, 4$) provide an insight into the local structure and bonding in the vicinity of rare earth ions. So the Judd–Ofelt analysis of the PL emission can be used for calculating the parity-forbidden electric-dipole radiative transition rates between the various levels of the rare earth ions.^{17,22} Through these analyses, the local environment around the metal ion and the bond covalency of metal–ligand bonds can be interpreted. The integrated emission intensities of the spontaneous (radiative) emission of the transition between two manifolds ⁵D₀ and ⁷F_{*j*} ($f = 2, 4$) were

Table 2 Absolute electronegativity, calculated CB edge, calculated VB position and band gap energy for Bi_{1-x}Eu_xOCl compounds

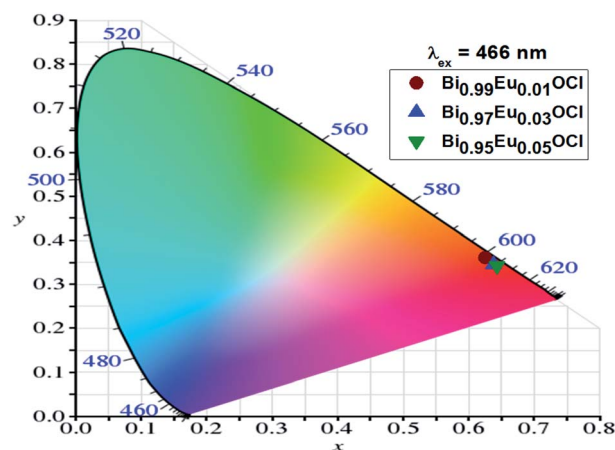
Compounds	Absolute electronegativity X (eV)	Calculated CB position (eV)	Calculated VB position (eV)	Band gap energy, E _g (eV)
BiOCl	6.34	0.38	3.30	2.92
Bi _{0.99} Eu _{0.01} OCl	6.34	0.39	3.29	2.90
Bi _{0.97} Eu _{0.03} OCl	6.34	0.40	3.28	2.88
Bi _{0.95} Eu _{0.05} OCl	6.34	0.41	3.27	2.86

**Fig. 7** (a) Excitation spectra of Bi_{0.99}Eu_{0.01}OCl phosphor (inset shows the magnified view of excitation spectra) and (b) emission spectra of Bi_{1-x}Eu_xOCl phosphors.

associated with the radiative emission rates and can be written as:

$$A_{0-J} = A_{0-1} \frac{I_{0-J}}{I_{0-1}} \frac{h\nu_{0-1}}{h\nu_{0-J}} \quad (5)$$

where I_{0-J} and I_{0-1} are integral intensities for $^5D_0 \rightarrow ^7F_J$ and $^5D_0 \rightarrow ^7F_1$ transitions and $h\nu_{0-J}$ and $h\nu_{0-1}$ are their energies, respectively. The magnetic dipole radiative emission rate A_{0-1} has a value of 50 s^{-1} .²³ The radiative emission rates A_{0-J} were related to forced electric dipole transitions and they may be written as a function of the J-O intensity parameters:

**Fig. 8** CIE 1931 chromaticity diagram of Bi_{1-x}Eu_xOCl phosphors.

$$A_{0-J} = \frac{64\pi^4(v_{0-J})^3 e^2}{3hc^3} \frac{1}{4\pi\epsilon_0} \chi \sum_{J=2,4} \Omega_J \langle ^5D_0 | U^{(J)} | ^7F_J \rangle^2 \quad (6)$$

where χ is the Lorentz local field correction factor given as function of the index of refraction n of the host $\chi = \frac{n(n^2 + 2)^2}{9}$. The $\langle ^5D_0 | U^{(J)} | ^7F_J \rangle^2$ are the square reduced matrix elements whose values are independent of the chemical environment of the Eu³⁺ ion. Their values were known and are $\langle ^5D_0 | U^{(2)} | ^7F_2 \rangle^2 = 0.0032$ and $\langle ^5D_0 | U^{(4)} | ^7F_4 \rangle^2 = 0.0023$. Thus, using eqn (5) and (6) the values of $\Omega_{2,4}$ were obtained. The calculated Judd–Ofelt parameters have been used to predict some important radiative properties such as radiative transition probability (A_{rad}) and lifetime (τ_{rad}).

The radiative transition probability (A_{rad}) can be calculated using the equation below:

$$A_{\text{rad}} = \sum_J A_{0-J} \quad (7)$$

The radiative lifetime τ_{rad} of an excited state in terms of A_{rad} , is given by:

$$\tau_{\text{rad}} = \frac{1}{A_{\text{rad}}} \quad (8)$$

The Judd–Ofelt intensity parameters, radiative transition probability and calculated lifetime of Bi_{1-x}Eu_xOCl phosphors are displayed in Table 3. The relative intensity of the hypersensitive electric dipole $^5D_0 \rightarrow ^7F_2$ transition depends on the

Table 3 Judd–Ofelt intensity parameters (Ω_2 , Ω_4), radiative transition probability (A_{rad}), non-radiative relaxation rate (W_{NR}), total transition probability (A_{tot}), calculated radiative (τ_{rad}) lifetime, experimental (τ_{exp}) lifetime, quantum efficiency (η) and asymmetry ratio of $\text{Bi}_{1-x}\text{Eu}_x\text{OCl}$ phosphors

Eu^{3+} (mol%)	J–O intensity parameters ($\times 10^{-20} \text{ cm}^2$)		$A_{\text{rad}} (\text{s}^{-1})$	$W_{\text{NR}} (\text{s}^{-1})$	$A_{\text{tot}} (\text{s}^{-1})$	$\tau_{\text{rad}} (\text{ms})$	$\tau_{\text{exp}}^a (\text{ms})$	$\eta (\%)$	Asymmetry ratio
	Ω_2	Ω_4							
1	1.4167	0.6861	191.98	22.19	214.17	5.21	4.67	90	1.77
3	1.5156	0.7454	203.05	5.95	209.00	4.92	4.78	97	2.06
5	1.5567	0.7506	205.68	1.71	207.39	4.86	4.82	99	2.09

^a Maximum experimental lifetime error: $\tau_{\text{exp}} = 0.0016 \text{ ms}$.

local symmetry of the Eu^{3+} ions. This transition was mainly responsible for the Ω_2 value, and it depends on short distance effects. The change of Ω_2 parameter was due to distortions around occupied Eu^{3+} ion sites. The intensity of this transition increases with decreasing local symmetry of the Eu^{3+} ion. It was observed that the value of Ω_2 parameter increases with increase in the Eu^{3+} concentration. This result reveals the high covalence of the metal–ligand bonds and more distortion of the symmetry of Eu^{3+} sites in BiOCl matrix.²⁴ The parameter Ω_4 was not directly related to the symmetry of the Eu^{3+} ion but to the electron density on the surrounding ligands. Its value increases with increase in the concentration of Eu^{3+} , indicating the decrease in the electron density on the ligands.

Asymmetric ratio was used to understand the variation of symmetry and coordination environment around Eu^{3+} ion doped in BiOCl matrix. The asymmetric ratio is a relative ratio of integrated areas under the peaks of $^5\text{D}_0 \rightarrow ^7\text{F}_2$ and $^5\text{D}_0 \rightarrow ^7\text{F}_1$ transitions.²⁵ In a site with inversion symmetry, the $^5\text{D}_0 \rightarrow ^7\text{F}_1$ transition was dominant while in a site without inversion symmetry, the $^5\text{D}_0 \rightarrow ^7\text{F}_2$ transition dominates. The asymmetric ratios for $\text{Bi}_{1-x}\text{Eu}_x\text{OCl}$ phosphors increase with increase in Eu^{3+} concentration (Table 3). This was due to the distortion in symmetry around Eu^{3+} ion in BiOCl which caused an enhancement in the relative intensity of the hypersensitive electric dipole transition. This indicates strong electric fields of low symmetry at the Eu^{3+} ions.

Fig. 9 shows the PL decay curve for $\text{Bi}_{1-x}\text{Eu}_x\text{OCl}$ phosphors measured at low temperature (77 K). The decay curve was monitored for the emission band at 620 nm, corresponding to the $^5\text{D}_0 \rightarrow ^7\text{F}_2$ transition, under the excitation of 466 nm. These PL decay profiles exhibit single exponential behavior and the excited state lifetime was calculated from the slope of the fitting line using the following expression:

$$I_t = I_0 e^{-t/\tau} \quad (9)$$

where I_t and I_0 are the luminescence intensities at time t and at $t = 0$ respectively, τ is the lifetime of the excited state energy level.

The experimental lifetime (τ_{exp}) values of the $^5\text{D}_0$ level of Eu^{3+} in BiOCl are presented in Table 3. These lifetime values support the increase in luminescence intensity of $^5\text{D}_0 \rightarrow ^7\text{F}_2$ transition in Eu^{3+} -activated BiOCl phosphors. It was obvious that the decay time increases with increase of Eu^{3+} ion concentration due to

the decrease in symmetry around Eu^{3+} ion.²⁶ It was observed that the experimental lifetime (τ_{exp}) values were lower than the calculated radiative lifetime (τ_{rad}) values. This was due to the non-radiative relaxation rate (W_{NR}) of the $^5\text{D}_0$ energy level of the Eu^{3+} ions which was determined by the relation:

$$W_{\text{NR}} = \frac{1}{\tau_{\text{exp}}} - \frac{1}{\tau_{\text{rad}}} \quad (10)$$

The total transition probability is the sum of radiative and non-radiative emission rates. Its value decreases with increase of Eu^{3+} concentration in BiOCl matrix due to the decrease in symmetry around Eu^{3+} ion (Table 3). Luminescence quantum efficiency (η) is defined as the ratio of number of photons emitted to the number of photons absorbed. But for the Ln^{3+} ion system, it is defined as the ratio of the experimental lifetime to the calculated radiative lifetime of the $^5\text{D}_0$ level and was measured from the following expression:

$$\eta(\%) = \frac{\tau_{\text{exp}}}{\tau_{\text{rad}}} \times 100 \quad (11)$$

The non-radiative relaxation rate and quantum efficiency of $\text{Bi}_{1-x}\text{Eu}_x\text{OCl}$ phosphors are shown in Table 3. The calculated W_{NR} values of the present phosphors were less than lead fluorophosphate²⁶ and telluro fluoroborate²⁷ glasses. Table 4 illustrates a comparison of the experimental lifetime and quantum efficiency for $^5\text{D}_0$ level of Eu^{3+} ion in BiOCl along with reported Eu^{3+} doped different host matrices. As can be seen from Table 4, it was found that the experimental lifetime and quantum efficiency of $\text{Bi}_{1-x}\text{Eu}_x\text{OCl}$ phosphors were higher than the Eu^{3+} doped LaOF ,²⁸ $\text{KLa}(\text{PO}_3)_4$,²⁹ $\text{KLu}(\text{WO}_4)_2$,³⁰ telluro fluoroborate,²⁷ lead fluorophosphate²⁶ and tellurite³¹ glass. The quantum efficiency of 99% of $^5\text{D}_0$ level suggests the efficiency of the $\text{Bi}_{0.95}\text{Eu}_{0.05}\text{OCl}$ phosphors as a potential host material for red laser applications.

The stimulated emission cross-section (σ_e) is an important factor to predict the laser performance of a material and also the rate of the energy extraction from the lasing material, and was calculated as

$$\sigma_e(\lambda_p) = \left[\frac{\lambda_p^4}{8\pi c n^2 \Delta \lambda_{\text{eff}}} \right] A_{0-j} \quad (12)$$

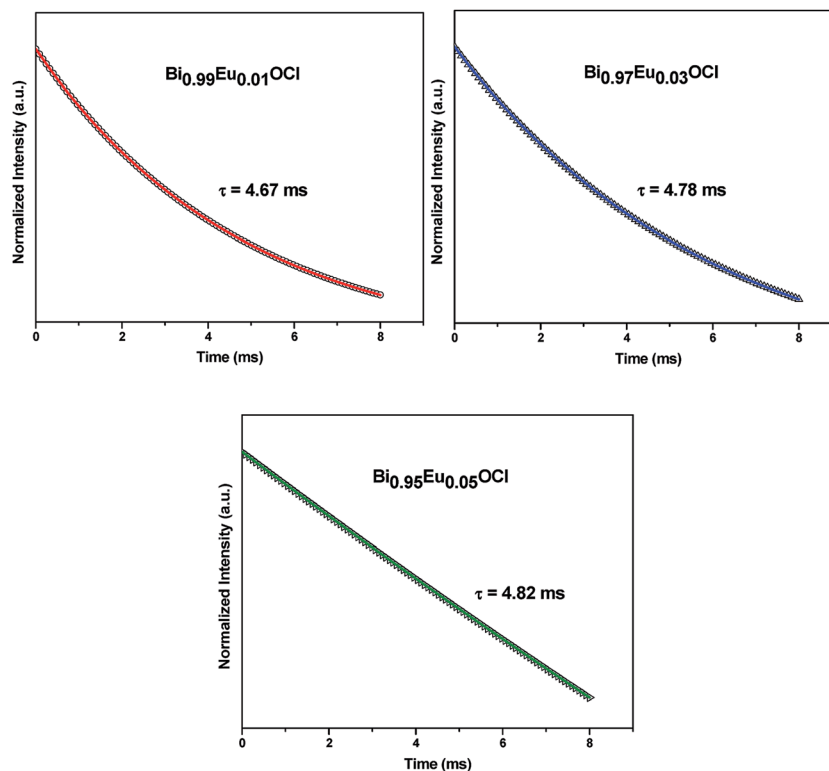


Fig. 9 Photoluminescence decay curve for the Eu^{3+} -activated BiOCl phosphors measured at 77 K with $\lambda_{\text{ex}} = 466$ nm and $\lambda_{\text{em}} = 620$ nm. The dots represent the observed points and the solid line gives its exponential fitting.

where λ_p is the emission peak wavelength, c is the velocity of light and $\Delta\lambda_{\text{eff}}$ is the effective bandwidth of the emission transition.

Some of the radiative properties such as the effective bandwidth of the emission transition ($\Delta\lambda_{\text{eff}}$), stimulated emission cross-section (σ_e), gain bandwidth ($\sigma_e \times \Delta\lambda_{\text{eff}}$) and optical gain ($\sigma_e \times \tau_{\text{exp}}$) for $\text{Bi}_{1-x}\text{Eu}_x\text{OCl}$ phosphors are displayed in Table 5. The trend of σ_e for the $^5\text{D}_0$ emission transition were observed as $^7\text{F}_2 > ^7\text{F}_4 > ^7\text{F}_1$ for Eu^{3+} -activated BiOCl phosphors. The

stimulated emission cross-section values of the prepared phosphors for $^5\text{D}_0 \rightarrow ^7\text{F}_2$ transition were found to be better than those reported for Eu^{3+} doped $\text{KLaEu}(\text{PO}_3)_4$,²⁹ Eu^{3+} doped ZnAlBiB (ref. 32) and Eu^{3+} ions in lithium aluminium borophosphate³³ glasses. The higher stimulated emission cross section value was an attractive feature for low threshold and high gain laser applications which were used to claim good laser action.²⁹ The product of emission cross-section and the effective bandwidth of the emission transition is a significant

Table 4 Comparison of experimental lifetime (τ_{exp}), quantum efficiency (η) of Eu^{3+} doped different host matrices

Host matrix	Eu^{3+} (mol%)	τ_{exp} (ms)	η (%)	Reference
BiOCl	1	4.67	90	Present work
	3	4.78	97	Present work
	5	4.82	99	Present work
LaOF	0.5	1.394	95	28
	20	0.427	24	28
$\text{KLa}(\text{PO}_3)_4$	2	3.45	66	29
	30	3.48	66	29
$\text{KLu}(\text{WO}_4)_2$	1	0.26	—	30
	1.5	0.68	—	30
	3	1.04	—	30
	5	1.29	72	30
	0.05	1.452	39	27
Telluro fluoroborate glass	1	1.601	63	27
	10	2.29	86	26
Lead fluorophosphate glass	0.5	0.82	64	31
	1.5	0.88	74	31

Table 5 Effective bandwidth of the emission transition ($\Delta\lambda_{\text{eff}}$), stimulated emission cross-section (σ_e), gain bandwidth ($\sigma_e \times \Delta\lambda_{\text{eff}}$) and optical gain ($\sigma_e \times \tau_{\text{exp}}$) for $\text{Bi}_{1-x}\text{Eu}_x\text{OCl}$ phosphors

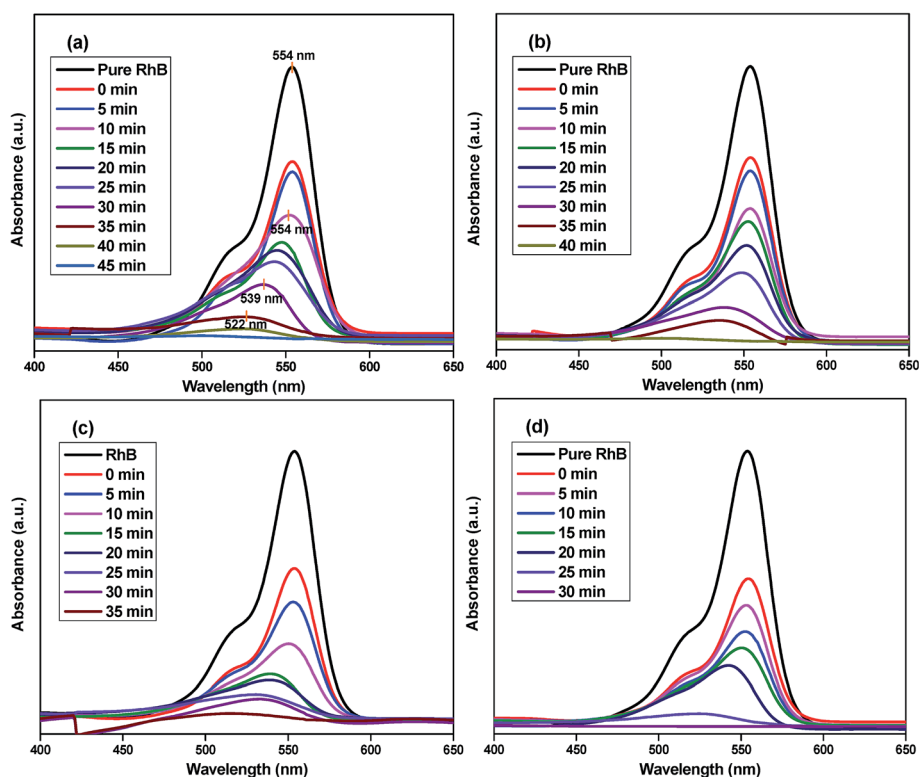
Eu^{3+} (mol%)	Transitions	$\Delta\lambda_{\text{eff}}$ (nm)	$\sigma_e (\times 10^{-22} \text{ cm}^2)$	$\sigma_e \times \Delta\lambda_{\text{eff}} (\times 10^{-28} \text{ cm}^3)$	$\sigma_e \times \tau_{\text{exp}} (\times 10^{-25} \text{ cm}^2 \text{ s}^{-1})$
1	$^5\text{D}_0 \rightarrow ^7\text{F}_1$	8.88	2.63	2.33	41.80
	$^5\text{D}_0 \rightarrow ^7\text{F}_2$	5.66	8.95	5.06	
	$^5\text{D}_0 \rightarrow ^7\text{F}_4$	5.40	7.43	4.01	
3	$^5\text{D}_0 \rightarrow ^7\text{F}_1$	7.83	2.98	2.34	45.31
	$^5\text{D}_0 \rightarrow ^7\text{F}_2$	5.87	9.48	5.56	
	$^5\text{D}_0 \rightarrow ^7\text{F}_4$	5.20	8.26	4.29	
5	$^5\text{D}_0 \rightarrow ^7\text{F}_1$	7.96	3.12	2.48	49.40
	$^5\text{D}_0 \rightarrow ^7\text{F}_2$	6.05	10.25	6.20	
	$^5\text{D}_0 \rightarrow ^7\text{F}_4$	5.37	9.27	4.98	

parameter to predict the bandwidth of the optical amplifier. The higher the product values were, the better was the amplifiers performance. It was noteworthy that the maximum value of gain bandwidth was $6.20 \times 10^{-28} \text{ cm}^3$ corresponding to $^5\text{D}_0 \rightarrow ^7\text{F}_2$ transition for $\text{Bi}_{0.95}\text{Eu}_{0.05}\text{OCl}$ phosphor. Similarly, the product of experimental lifetime and stimulated emission cross section is a vital aspect for high optical amplifier gain. The obtained gain bandwidth and optical gain values corresponding to $^5\text{D}_0 \rightarrow ^7\text{F}_2$ transition were found to be larger than Eu^{3+} doped ZnAlBiB (ref. 32) glass. Therefore, we can conclude that the $^5\text{D}_0 \rightarrow ^7\text{F}_2$ transition (620 nm) provide favorable lasing action, high gain bandwidth and optical gain for amplifiers. The large values of lifetime, stimulated emission cross-section, gain bandwidth

and optical gain suggest that the Eu^{3+} -activated BiOCl phosphors can be useful for red laser applications and also for the development of color display devices.

3.8. Photocatalytic activity

Fig. 10 shows the photocatalytic degradation of RhB dye over $\text{Bi}_{1-x}\text{Eu}_x\text{OCl}$ catalysts by monitoring the temporal changes of UV-Vis absorbance spectra. A significant reduction in maximum absorption spectra of RhB aqueous solution was verified during the photodegradation process. Before irradiation, the N,N,N',N' -tetra-ethylated rhodamine molecule, RhB dye, has one band with a maximum absorption centered at $\lambda_{\text{max}} = 554 \text{ nm}$. Visible light irradiation of the aqueous RhB/ $\text{Bi}_{1-x}\text{Eu}_x\text{OCl}$ dispersion

**Fig. 10** UV-Vis absorbance spectra of RhB dye as a function of time over (a) BiOCl , (b) $\text{Bi}_{0.99}\text{Eu}_{0.01}\text{OCl}$, (c) $\text{Bi}_{0.97}\text{Eu}_{0.03}\text{OCl}$ and (d) $\text{Bi}_{0.95}\text{Eu}_{0.05}\text{OCl}$ catalysts under visible illumination.

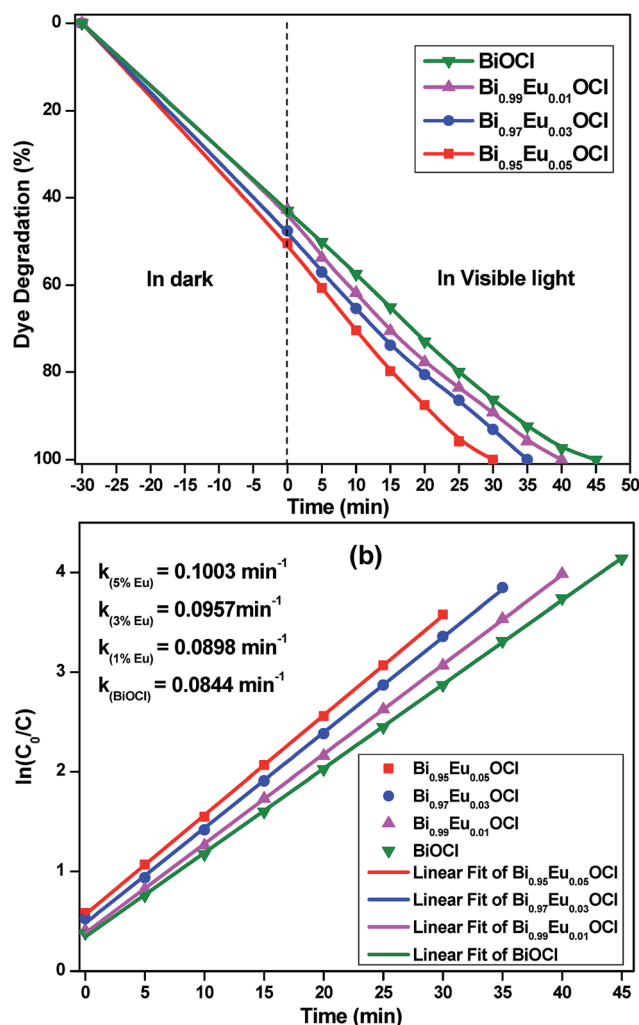


Fig. 11 (a) Percentage of RhB dye degradation and (b) first order kinetics of dye degradation over Bi_{1-x}Eu_xOCl catalysts as a function of irradiation time.

leads to a decrease in absorption with a concomitant wavelength shift of the band to shorter wavelengths. The blue shift depicted in Fig. 10 was caused by de-ethylation of RhB due to an attack by one of the active oxygen species on the *N*-ethyl group.³⁴ The shifting of the maximum absorption of RhB dye to other wavelength positions of its major absorption band which moved toward the *N,N,N'*-tri-ethylated rhodamine ($\lambda_{\text{max}} = 539 \text{ nm}$); *N,N'*-di-ethylated rhodamine, ($\lambda_{\text{max}} = 522 \text{ nm}$); *N*-ethylated rhodamine, ($\lambda_{\text{max}} = 510 \text{ nm}$) and rhodamine ($\lambda_{\text{max}} = 498 \text{ nm}$) species.³⁵ In the process of photodegradation, the intensity of the main peak reduced gradually to zero at 45 min (BiOCl), 40 min (Bi_{0.99}Eu_{0.01}OCl), 35 min (Bi_{0.97}Eu_{0.03}OCl) and 30 min (Bi_{0.95}Eu_{0.05}OCl). This revealed that the molecular structure of RhB was decomposed to yield environmental friendly species. Fig. 11a shows the percentage of dye degradation after irradiation for different times. When the reaction was performed under dark for 30 min, we observed 42%, 44%, 48% and 51% RhB dye degradation for Bi_{1-x}Eu_xOCl ($x = 0, 0.01, 0.03$ and 0.05) catalysts, respectively. This shows that the Bi_{0.95}Eu_{0.05}OCl

catalyst has good adsorption capacity. Under visible illumination, the 100% RhB dye was decomposed within 45, 40, 35 and 30 min for Bi_{1-x}Eu_xOCl ($x = 0, 0.01, 0.03$ and 0.05) catalysts, respectively.

To prove the efficiency of Bi_{1-x}Eu_xOCl catalysts with the possibility for future industrial applications, the reaction kinetics was evaluated. The kinetics of RhB degradation reaction under visible light is presented in Fig. 11b, which follows apparent first order kinetics in agreement with a general Langmuir-Hinshelwood mechanism³⁶

$$R = \frac{-dC}{dt} = \frac{kKC}{1 + KC} \quad (13)$$

where R is the degradation rate of reactant ($\text{mg L}^{-1} \text{ min}^{-1}$), C is the concentration of reactant (mg L^{-1}), t is the illumination time, K is the adsorption coefficient of reactant (L mg^{-1}) and k is the reaction rate constant. If C is very small then the above equation could be simplified to

$$\ln\left(\frac{C_0}{C}\right) = kKt = k_{app}t \quad (14)$$

where C_0 is the initial concentration (0 min) of the RhB aqueous solution and C is the concentration of the RhB aqueous solution for different times of visible illumination.

According to eqn (14), if $\ln(C_0/C)$ was plotted as a function of t , a straight line was observed, whose slope is equal to the apparent first-order rate constant k_{app} which were calculated to be 0.0844, 0.0898, 0.0957 and 0.1003 min^{-1} for Bi_{1-x}Eu_xOCl ($x = 0, 0.01, 0.03$ and 0.05) catalysts, respectively. These values substantiate the photocatalytic reaction rate being highest for Bi_{0.95}Eu_{0.05}OCl catalyst. Further, the rate constants increase with increase in Eu³⁺ doping concentration for Bi_{1-x}Eu_xOCl catalysts. This was due to the decrease in band gap energy values with Eu³⁺ doping concentration. The indirect optical transition and layered structure of BiOCl play an important role in its excellent photocatalytic activity. In indirect transition, an excited electron has to travel certain k -space distance to reach valence band. This reduces the recombination probability of the excited electron and the hole. The layered structure of BiOCl can polarize the related atoms and orbitals by supporting large enough space,¹⁰ resulting in an increase in the electron-hole separation efficiency through the appeared dipole, and thus the enhanced photocatalytic activity was observed.

4. Conclusions

Layered Bi_{1-x}Eu_xOCl compounds were prepared by conventional solid-state method at relatively low temperature. Rietveld refinement results confirmed that these compounds have a tetragonal structure. Based on the CIE chromaticity diagram, the Eu³⁺-activated BiOCl phosphors exhibit red luminescence under visible excitation. In order to investigate the nature of the luminescence behavior of Eu³⁺ in BiOCl, the Judd-Ofelt intensity parameters were calculated from the emission data. The J-O intensity parameters increase with the increase in Eu³⁺ concentration which reveals the high covalence of the metal-ligand bonds and more distortion of the symmetry of Eu³⁺ sites

in BiOCl matrix. The high asymmetric ratio confirmed that the Eu^{3+} ions locate at sites with low symmetry and without an inversion center. The present Eu^{3+} -activated BiOCl phosphors show higher lifetime, quantum efficiency, stimulated emission cross-section, gain bandwidth and optical gain parameters for $^5\text{D}_0 \rightarrow ^7\text{F}_2$ transition in comparison with different host matrix such as oxides and glasses. We achieved 100% RhB dye degradation using $\text{Bi}_{1-x}\text{Eu}_x\text{OCl}$ ($x = 0, 0.01, 0.03$ and 0.05) catalysts within 45, 40, 35 and 30 min under visible illumination. The apparent first-order rate constant was found to be in the decreasing order of $\text{Bi}_{0.95}\text{Eu}_{0.05}\text{OCl} > \text{Bi}_{0.97}\text{Eu}_{0.03}\text{OCl} > \text{Bi}_{0.99}\text{Eu}_{0.01}\text{OCl} > \text{BiOCl}$ which followed the 1st order kinetic mechanism. The high efficiency was ascribed to their indirect band gap, layered structure and ability to utilize broad bands in the solar spectrum. The present work provides an effective and economic material ideal for developing red component in white LEDs, red lasers and environment remedy applications.

Acknowledgements

Authors are thankful to DST-IRHPA for FESEM and EDX facility. One of the author R. Saraf would like to thank Indian Academy of Sciences for awarding summer research fellowship 2014.

References

- 1 S. Cho, R. Lee, H. Lee, J. Kim, C. Moon, S. Nam and J. Park, *J. Sol-Gel Sci. Technol.*, 2010, **53**, 171.
- 2 J. Wang, Y. Xu, M. Hojamberdiev, J. Peng and G. Zhu, *J. Non-Cryst. Solids*, 2009, **355**, 903.
- 3 G. G. Li, D. L. Geng, M. M. Shang, Y. Zhang, C. Peng, Z. Y. Cheng and J. Lin, *J. Phys. Chem. C*, 2011, **115**, 21882.
- 4 A. Dash, S. Sarkar, V. N. Adusumalli and V. Mahalingam, *Langmuir*, 2014, **30**, 1401.
- 5 X. Zhang, Z. Ai, F. Jia and L. Zhang, *J. Phys. Chem. C*, 2008, **112**, 747.
- 6 Q. Wang, J. Hui, Y. Huang, Y. Ding, Y. Cai, S. Yin, Z. Li and B. Su, *Mater. Sci. Semicond. Process.*, 2014, **17**, 87.
- 7 H. L. Peng, C. K. Chan, S. Meister, X. F. Zhang and Y. Cui, *Chem. Mater.*, 2009, **21**, 247.
- 8 W. L. Huang and Q. Zhu, *J. Comput. Chem.*, 2009, **30**, 183.
- 9 D. K. Li, L. Z. Pei, Y. Yang, Y. Q. Pei, Y. K. Xie and Q. F. Zhang, *e-J. Surf. Sci. Nanotechnol.*, 2012, **10**, 161.
- 10 K. L. Zhang, C. M. Liu, F. Q. Huang, W. D. Wang and J. L. Shi, *Appl. Catal., B*, 2006, **68**, 125.
- 11 Y. Q. Lei, G. H. Wang, S. Y. Song, W. Q. Fan and H. J. Zhang, *CrystEngComm*, 2009, **11**, 1857.
- 12 J. Henle, P. Simon, A. Frenzel, S. Scholz and S. Kaskel, *Chem. Mater.*, 2007, **19**, 366.
- 13 J. Tauc, *Optical Properties of Solids*, North-Holland, Amsterdam, 1970.
- 14 W. L. Huang and Q. Zhu, *Comput. Mater. Sci.*, 2008, **43**, 1101.
- 15 L. Chen, S. F. Yin, R. Huang, Y. Zhou, S. L. Luo and C. T. Au, *Catal. Commun.*, 2012, **23**, 54.
- 16 Y. Hui, Y. Zhao, S. Zhao, L. Gu, X. Fan, L. Zhu, B. Zou, Y. Wang and X. Cao, *J. Alloys Compd.*, 2013, **573**, 177.
- 17 G. S. Ofelt, *J. Chem. Phys.*, 1962, **37**, 511.
- 18 R. Saraf, C. Shivakumara, N. Dhananjaya, S. Behera and H. Nagabhushana, *J. Mater. Sci.*, 2015, **50**, 287.
- 19 S. Shionoya and W. M. Yen, *Phosphor Handbook*, Phosphor Research Society, CRC Press, 1998.
- 20 *Color calculator version 2*, A software from, Radiant Imaging, Inc, 2007.
- 21 C. H. Huang, T. W. Kuo and T. M. Chen, *Opt. Express*, 2011, **19**, A1.
- 22 B. R. Judd, *Phys. Rev.*, 1962, **127**, 750.
- 23 G. F. de Sá, O. L. Malta, C. M. Donegá, A. M. Simas, R. L. Longo, P. A. Santa-Cruz and E. F. da Silva, *Coord. Chem. Rev.*, 2000, **196**, 165.
- 24 R. Reisfeld, E. Zigansky and M. Gaft, *Mol. Phys.*, 2004, **102**, 1319.
- 25 A. M. Cross, P. S. May, F. C. J. M. van Veggel and M. T. Berry, *J. Phys. Chem. C*, 2010, **114**, 14740.
- 26 C. R. Kesavulu, K. K. Kumar, N. Vijaya, K. S. Lim and C. K. Jayasankar, *Mater. Chem. Phys.*, 2013, **141**, 903.
- 27 R. Vijayakumar, K. Maheshvaran, V. Sudarsan and K. Marimuthu, *J. Lumin.*, 2014, **154**, 160.
- 28 T. Grzyb and S. Lis, *Inorg. Chem.*, 2011, **50**, 8112.
- 29 M. Ferhi, C. Bouzidi, K. H. Naifer, H. Elhouichet and M. Ferid, *J. Lumin.*, 2015, **157**, 21.
- 30 M. C. Pujol, J. J. Carvajal, X. Mateos, R. Sole, J. Massons, M. Aguilo and F. Diaz, *J. Lumin.*, 2013, **138**, 77.
- 31 W. Stambouli, H. Elhouichet, B. Gelloz and M. Ferid, *J. Lumin.*, 2013, **138**, 201.
- 32 K. Swapna, S. Mahamuda, A. S. Rao, T. Sasikala, P. Packiyaraj, L. R. Moorthy and G. V. Prakash, *J. Lumin.*, 2014, **156**, 80.
- 33 P. S. Wong, M. H. Wan, R. Hussin, H. O. Lintang and S. Endud, *J. Rare Earths*, 2014, **32**, 585.
- 34 Y. Zhao, C. Li, X. Liu and F. Gu, *J. Alloys Compd.*, 2007, **440**, 281.
- 35 T. Wu, G. Liu, J. Zhao, H. Hidaka and N. Serpone, *J. Phys. Chem. B*, 1998, **102**, 5845.
- 36 D. F. Ollis, *J. Phys. Chem. B*, 2005, **109**, 2439.